IOP Publishing and International Atomic Energy Agency Nuclear Fusion

Nucl. Fusion **48** (2008) 084001 (13pp) doi:10.1088/0029-5515/48/8/084001

Central flattening of the fast-ion profile in reversed-shear DIII-D discharges

W.W. Heidbrink[1], M.A. Van Zeeland[2], M.E. Austin[3], K.H. Burrell[2], N.N. Gorelenkov[4], G.J. Kramer[4], Y. Luo[1], M.A. Makowski[5], G.R. McKee[6], C. Muscatello[1], R. Nazikian[4], E. Ruskov[1], W.M. Solomon[4], R.B. White[4] and Y. Zhu[1]

[1] University of California, Irvine, CA 92697, USA
[2] General Atomics, PO Box 85608, San Diego, CA 92186, USA
[3] University of Texas, Austin, TX 78712, USA
[4] Princeton Plasma Physics Laboratory, Princeton, NJ 08543, USA
[5] Lawrence Livermore National Laboratory, Livermore, CA 94550, USA
[6] University of Wisconsin, Madison, WI 53706, USA

Received 1 December 2007, accepted for publication 8 February 2008
Published 26 June 2008
Online at stacks.iop.org/NF/48/084001

Abstract
Neutral beam injection into a plasma with negative central shear produces a rich spectrum of toroidicity-induced and reversed-shear Alfvén eigenmodes in the DIII-D tokamak. The application of fast-ion D_α (FIDA) spectroscopy shows that the central fast-ion profile is flattened in the inner half of the discharge. Neutron and equilibrium measurements corroborate the FIDA data. The temporal evolution of the current profile is also strongly modified. Studies in similar discharges show that flattening of the profile correlates with the mode amplitude and that both types of Alfvén modes correlate with fast-ion transport. Calculations by the ORBIT code do *not* explain the observed fast-ion transport for the measured mode amplitudes, however. Possible explanations for the discrepancy are considered.

PACS numbers: 52.55.Pi, 52.35.Bj, 52.55.Fa

(Some figures in this article are in colour only in the electronic version)

1. Introduction

Alpha particles produced in deuterium–tritium fusion reactions may drive Alfvén eigenmodes unstable in ITER and other burning plasma experiments [1]. If they do, the most important practical issue is the resultant fast-ion transport. Will the alphas escape from the plasma and damage the first wall? Even if losses are minimal, how will redistribution of the alpha heating alter plasma performance? The expulsion of fast ions by toroidicity-induced Alfvén eigenmodes (TAE) [2] coated optical components with ablated carbon in the DIII-D tokamak [3] and created a vacuum leak in the tokamak fusion test reactor (TFTR) [4]. The damage was explained qualitatively in terms of wave–particle resonances and orbital effects but no quantitative comparisons between the measured fluctuation levels and the expected transport were given in these publications. In the only quantitative comparisons between theory and experiment [5–7], wave amplitudes an order of magnitude larger than the measured values were needed to predict the large losses observed experimentally.

The fast-ion and instability diagnostics were less extensive in these early studies, suggesting that misinterpretation of the available signals might account for the discrepancy. In the work reported here, however, both the instabilities and the fast-ion response are very well characterized. Nevertheless, the calculated fast-ion transport is still much smaller than the observed value.

Highlights of this new work were recently published in a brief letter [7]. In this paper, many more experimental details are provided; in addition, new data from similar discharges are included. These new data clearly show that both TAEs and reversed shear Alfvén eigenmodes (RSAEs) [8] affect fast-ion transport. (RSAEs are also known as 'Alfvén cascades'.) Additional information about the comparison with theory is also given, as well as a more extensive discussion of possible reasons for the discrepancy.

The paper begins with a description of the plasma conditions and diagnostics (section 2). Measurements of fast-ion transport in the baseline discharge (section 3.1), in recent discharges with electron cyclotron heating (section 3.2), and the correlation of fast-ion transport with mode activity (section 3.3) appear next. Section 4 describes the simulation results. Possible explanations for the discrepancy are evaluated in section 5, followed by the conclusions (section 6).

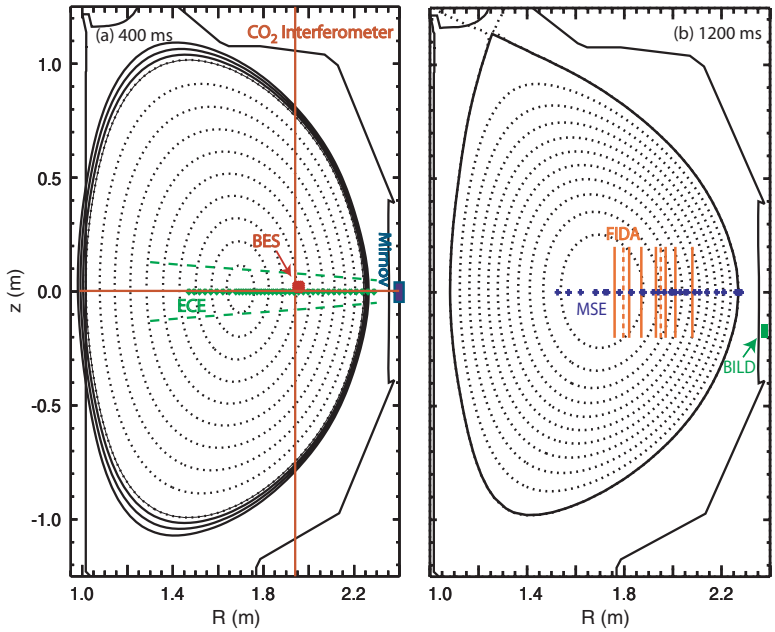

Figure 1. Elevation of the DIII-D vessel showing equilibrium flux surfaces from EFIT [25] reconstructions at (*a*) 400 ms and (*b*) 1200 ms in the baseline discharge, #122117. (*a*) Fluctuation diagnostics. The radial locations of the 40 ECE channels are represented by green points and the ECE beam waist is represented by dashed green lines. On shot #122117, the 4 × 4 array of high-resolution BES channels (large point) was located at the indicated location (near $\rho_{q_{\min}}$). The two interferometer channels used for global cross-power measurements are also indicated. The magnetics data in this paper come from a Mirnov coil mounted on the outer wall at the midplane. (*b*) Fast-ion diagnostics. The radial locations of the MSE channels used in the equilibrium reconstructions are indicated by + symbols. FIDA channels are represented by orange lines; the vertical extent is the vertical footprint of the injected beam; the dashed lines represent the locations measured by the dedicated instrument [22] that measures full spectra with 1 ms temporal resolution. The beam-ion loss detector (BILD) is mounted near the indicated location.

2. Plasma conditions and diagnostics

The experiments were performed in the DIII-D tokamak (major radius $R_0 \simeq 1.7$ m, minor radius $a \simeq 0.6$ m, graphite walls, deuterium plasmas) during the 2005–2007 campaigns. For all of the discharges discussed here, the beams inject 75–81 keV deuterium beam ions in the direction of the plasma current (co-injection). Generally, the beams are injected at a tangency radius of 1.15 m, although a few discharges have a modest fraction of the power injected at $R_{\tan} = 0.76$ m. The plasmas are limited on the inner wall for the first ∼125 ms of beam injection (figure 1(*a*)) and then become an upwardly biased divertor configuration (figure 1(*b*)). In this configuration, the plasma remains in L-mode during the time of interest.

In the baseline discharge (#122117) (figure 2), 4.6 MW of 80 keV deuterium neutral beams are injected in the direction of the plasma current into a low-density ($\bar{n}_e = 2 \times 10^{13}$ cm^{-3}), deuterium plasma with central $T_e = 1$–2 keV. The beams are injected early in the plasma current ramp to produce a reversed-shear plasma with an off-axis minimum in the safety factor q at $\rho_{q_{\min}}$. (The normalized minor radius coordinate is proportional to the square root of the toroidal flux ρ.) The central beam pressure is large (∼50% of the total) and the ratio of the injected beam speed v to the Alfvén speed v_A is ∼0.45. At the magnetic axis, the peak of the fast-ion distribution function occurs at a pitch of $v_\parallel/v = 0.68$, so an appreciable fraction of the fast-ion distribution can resonate with a TAE at $v_\parallel = v_A/3$ [9, 10]. Figure 3 shows representative electron temperature profiles from Thomson scattering [11] and electron cyclotron emission (ECE) [12] diagnostics, electron density from Thomson scattering and CO_2 interferometry [13], and ion temperature, toroidal rotation, and carbon density profiles from charge-exchange recombination spectroscopy [14]. The dominant impurity is carbon in these discharges and $Z_{\text{eff}} \simeq 1.3$. These q and density profiles produce a large, open, toroidicity-induced gap in the Alfvén continuum (figure 3 of [15]).

Many instruments diagnose the fast ions (figure 1(*b*)). As discussed extensively in [16], these different instruments weight the fast-ion distribution function differently in velocity space. A plastic scintillator that is cross-calibrated to an absolutely calibrated fission counter measures the volume-averaged 2.5 MeV neutron rate [17]. In these plasmas, the neutron rate is dominated by beam–plasma reactions. (TRANSP [18] computes that ∼80% of the reactions are from beam–plasma, while most of the remainder are from beam–beam reactions.) The velocity-space weighting of the neutron measurement increases rapidly with energy because the d–d fusion cross section increases rapidly with energy, resulting in a signal that arises primarily from fast ions near the injection energy. There was a problem with the absolute calibration of the neutron diagnostic during the 2005 campaign: the measured neutron rate in quiet plasmas generally exceeds the classically predicted rate by 25–30%. This discrepancy is larger than the estimated ∼15% uncertainty in the absolute calibration [17] and is not observed in earlier or later years. Accordingly, in this paper, we interpret the discrepancy as an unresolved error in the absolute calibration. Neutron data from 2005 are normalized to the classically expected rate during a phase of a one-source discharge (#122116) without appreciable MHD (only modest sawtooth activity). For the

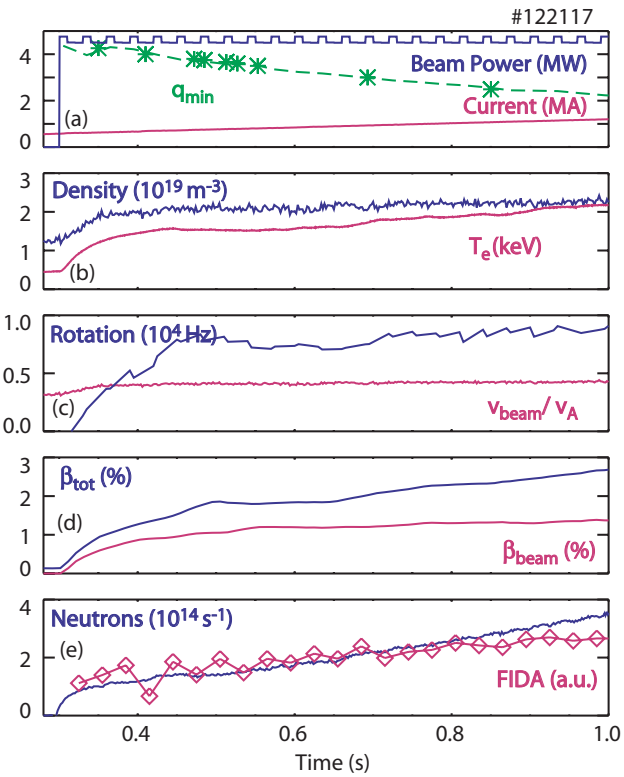

Figure 2. Time evolution of (*a*) neutral beam power, plasma current, and q_{min} inferred from the RSAE cascades, (*b*) line-average electron density $\bar{n}_e$ and central electron temperature, (*c*) central toroidal rotation from charge-exchange recombination spectroscopy of carbon impurities and ratio of the speed of injected 81 keV deuterium ions to the Alfvén speed evaluated using the vacuum magnetic field (2.0 T) and $\bar{n}_e$, (*d*) central toroidal beta and central beam-ion beta from TRANSP assuming neoclassical fast-ion behaviour and (*e*) measured neutron rate and FIDA density at 1.94 m in the baseline discharge.

2006–07 data, the usual calibration derived from the Cf^{252} radioactive source [17] (which is consistent with classical calculations in quiet plasmas) is employed. To isolate effects caused by the instabilities, the neutron signals are usually normalized to the classically expected rate as calculated by TRANSP. Although the absolute uncertainty in the normalized rate is $\gtrsim$20%, the relative uncertainty within a discharge (or when comparing sequential discharges) is considerably smaller ($\lesssim$10%), approximately the relative uncertainty in the electron temperature.

The primary fast-ion profile diagnostic is FIDA. Beam modulation and fitting of impurity lines is used to extract the fast-ion spectra from the interfering background light [19]; uncertainties in background subtraction are the dominant source of error and are represented by error bars in the figures. In this paper, the spectra are usually averaged over wavelength for improved statistics. The wavelength bin is specified in terms of energy E_λ along the (nearly vertical) viewing chord. In reality, since the photon Doppler shift is only determined by one component of the velocity, the diagnostic performs an effective average in velocity space over this and higher energies [16, 19, 20]. For the wavelengths employed in this paper (E_λ = 30–60 keV), the diagnostic effectively averages over the bulk of the fast-ion distribution function above the half-energy [16]. Since the signals are proportional to the product of the injected neutral density and the fast-ion density, the wavelength-integrated signals are usually divided by the injected neutral density (as calculated by a pencil-beam neutral deposition code [21]) to yield 'FIDA density' measurements over the high-energy portion of velocity space. Two different instruments are employed. One of these [22] measures spectra at two spatial locations with a high quantum efficiency CCD camera. The second instrument has seven spatial channels but only measures a portion of the spectrum (on the blue-shifted side) with slower, noisier Reticon photodiode detectors during the 2005 campaign and a high quantum efficiency CCD camera during the 2006–07 campaigns. The radial locations of the 9 spatial channels are illustrated in figure 1(*b*). The radial resolution of the measurement is quite good (a few centimetres) [19]; the vertical resolution of the measurement is determined by the vertical height of the injected-neutral footprint, which is about 40 cm centred on the midplane. In MHD-quiescent plasmas, the absolute magnitude of the spectra from the CCD channels is in excellent agreement with simulations that employ the TRANSP fast-ion distribution function but the absolute profile for the Reticon detectors is inconsistent with theory [23]. In contrast, relative changes in spatial profile are in excellent agreement with theory for both systems [23]. Changes in profile shape during acceleration of fast ions by fourth and fifth harmonic ion cyclotron heating are also consistent with theoretical predictions [16], so the FIDA technique has been thoroughly validated.

Additional information about the fast-ion profile is obtained from equilibrium reconstructions that rely on motional Stark effect (MSE) [24] measurements of the internal magnetic field (figure 1(*b*)). The profile of the total plasma pressure p_{tot} is obtained from EFIT [25] reconstructions of the MHD equilibrium that are consistent with the MSE data, with external magnetics data, and with isotherms of the electron temperature as measured by a 40-channel electron cyclotron emission (ECE) [12] radiometer (figure 1(*a*)). The thermal pressure p_{th} from the T_e, n_e, T_i and carbon density measurements (figure 3) is subtracted from the MHD pressure profile to obtain the fast-ion pressure profile p_f (figure 4) [26, 27]. The uncertainty in p_f is affected by both the uncertainty in the total pressure and the uncertainty in thermal pressure. The uncertainty in p_{th} is readily computed by propagating the estimated random errors in the thermal density and temperature measurements. The uncertainty in p_{tot} is more difficult to quantify because systematic errors in the EFIT equilibrium reconstruction exceed the errors associated with MSE, ECE and magnetics measurement errors. For the case shown here, the absolute uncertainty in the fast-ion pressure is $\sim$16% at $\rho = 0.25$ (with δp_{tot} and δn_e making the dominant contributions), while the relative uncertainty when comparing the profiles at different times in the same discharge is $\sim$10%. This fast-ion pressure measurement weights parallel pressure more heavily than perpendicular pressure but, ultimately, like the FIDA and neutron techniques, the measurement performs an effective average over the bulk of the fast-ion distribution function [16].

The equilibrium reconstructions also provide information about the current profile. Figure 5(*a*) shows the classically expected contributions to the current profile as calculated by

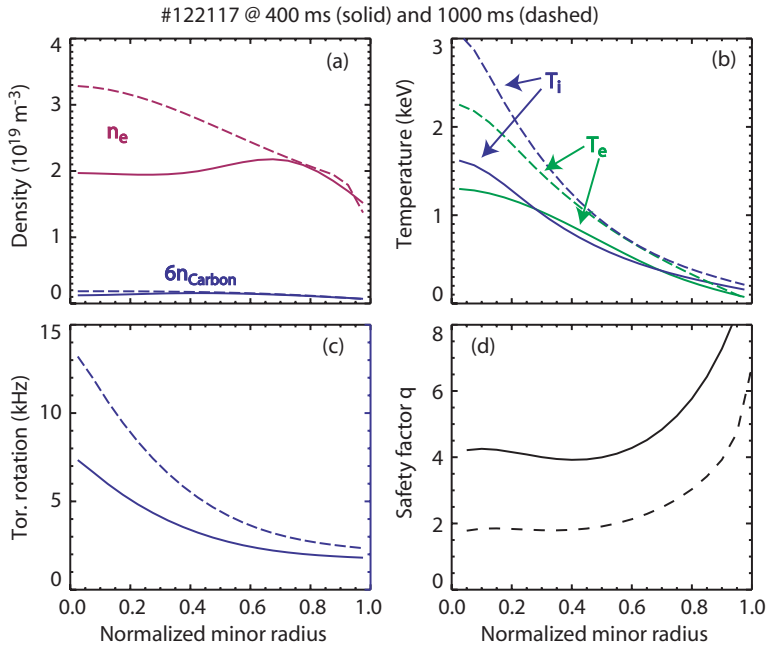

Figure 3. Profiles of (*a*) electron density and six times the carbon density, (*b*) electron and ion temperature, (*c*) toroidal rotation and (*d*) q profile versus normalized radius ρ at 400 ms (solid lines) and 1000 ms (dashed lines).

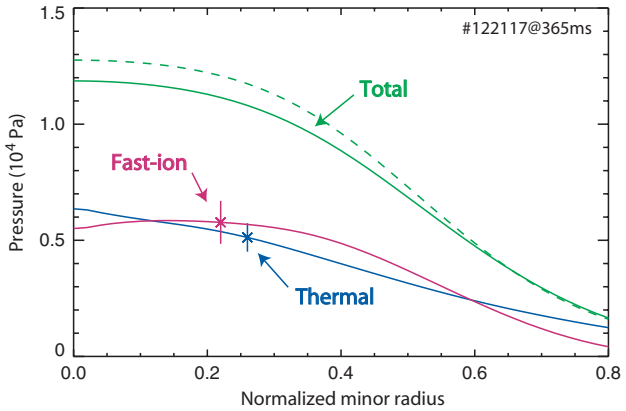

Figure 4. Total plasma pressure versus ρ from a MSE-based EFIT reconstruction (solid line) in the baseline discharge. The dashed line shows an alternative EFIT reconstruction that is barely consistent with the available experimental data. The thermal pressure profile (blue line) and inferred fast-ion pressure profile (red line) are also shown. The error bars represent typical uncertainties calculated using the procedure described in the appendix of [16].

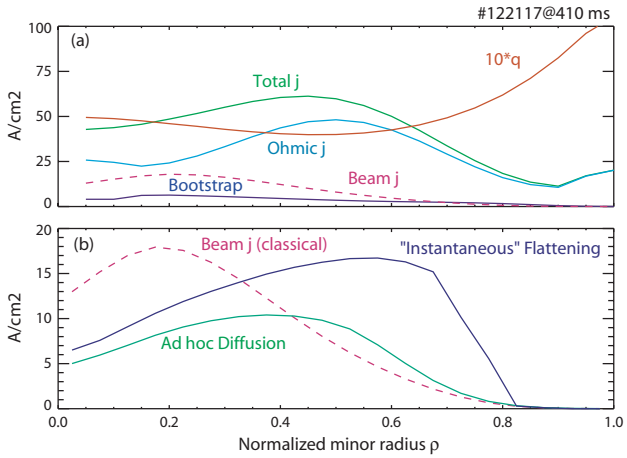

Figure 5. (*a*) Total (green), ohmic (blue), bootstrap (purple) and beam (dashed) current profiles as computed by TRANSP in the baseline discharge. The equilibrium and q profile (orange) are from EFIT. This TRANSP simulation assumes neoclassical resistivity and classical NBCD. (*b*) NBCD profiles under three different assumptions: classical (dashed), *ad hoc* D_B profile that is large in the core and small outside (green), and the NBCD profile that is expected if the fast ions quickly redistribute (relative to a slowing-down time) to a flat fast-ion density profile similar to the one shown in figure 8.

TRANSP during the ramp-up phase of the baseline discharge (#122117). Beam-driven currents constitute $\lesssim$25% of the total. Deviations of the observed current profile from the classically expected profile provides information on the circulating fast ions that contribute to neutral-beam current drive (NBCD). In addition to the evolution of q_{min} inferred from the equilibrium reconstructions, rational values of q_{min} are also inferred from the 'Alfvén cascades', i.e. the temporal pattern of frequency-sweeping RSAEs with different toroidal mode numbers [8].

Direct measurements of fast-ion losses are available from a pair of foils that are mounted ~12 cm below the midplane at the edges of a vacuum port (figure 1(*b*)) [28]. The apertures of these foils restrict the pitch angle of incident ions to either co-going or counter-going fast ions and restrict the energy to >10 keV. During these experiments, the bandwidth of the electronics was too low to detect coherent losses at the RSAE and TAE frequencies. In these discharges, non-zero signals are sometimes observed on the foil that measures ions moving toroidally in the direction of the plasma current. It should be noted that, because the detector is toroidally and poloidally localized, the absence of signals on the loss detectors does not necessarily imply the absence of losses everywhere.

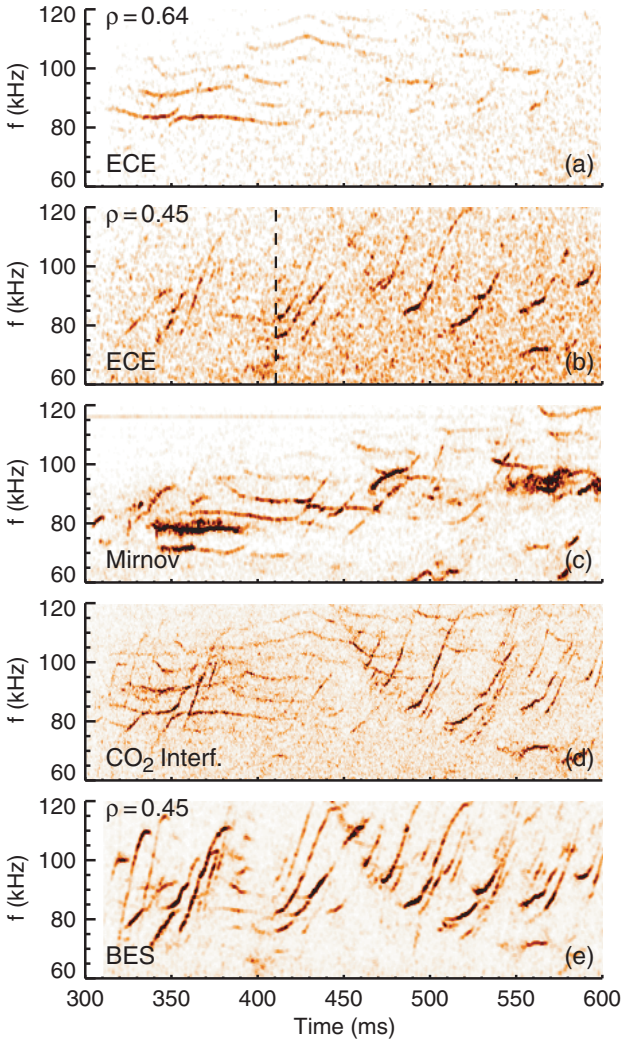

Figure 6. Spectra from several fluctuation diagnostics. (*a*) Power spectrum of ECE radiometer data for the channel that is at a radial position of $\rho = 0.64$. (*b*) Power spectrum of ECE radiometer data for the $\rho = 0.45$ channel. (*c*) Mirnov coil power spectrum. (*d*) Interferometer cross-power spectrum. (*e*) BES cross-power spectrum of adjacent channels that are near $\rho = 0.45$.

The DIII-D tokamak has an extensive suite of fluctuation diagnostics with the bandwidth and sensitivity needed to detect Alfvén instabilities (figure 1(*a*)). The 40-channel ECE radiometer measures electron temperature fluctuations [12], density fluctuations are measured by reflectometry [29], beam-emission spectroscopy (BES) [30] and CO_2 interferometry [31], and magnetic fluctuations are measured by Mirnov coils [32]. Figure 6 shows a sample of the spectra measured by several of these diagnostics in the baseline discharge. The modes that sweep up rapidly in frequency are RSAEs and the relatively steady modes are TAEs. Because the RSAEs and TAEs have differing spatial structures, the spectra differ markedly, particularly for the spatially localized ECE and BES diagnostics. For channels near the minimum q radius, the spectra are dominated by RSAEs (figures 6(*b*) and (*e*)) while, for localized channels away from $\rho_{q_{\min}}$, the TAEs dominate (figure 6(*a*)). The Mirnov signal is most sensitive to spatially extended modes; however both TAEs and RSAEs are apparent in the spectrum because the RSAE and TAE mode

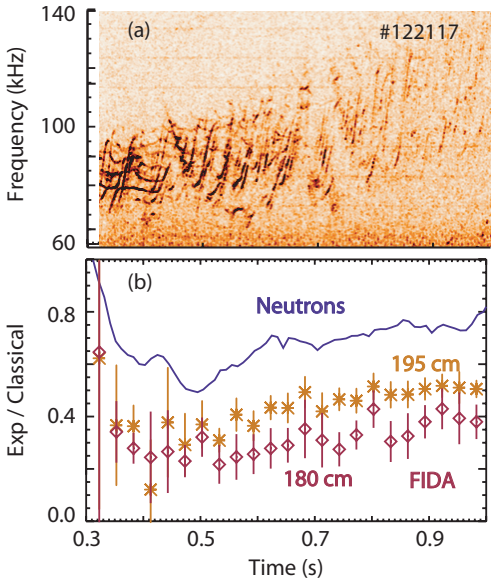

Figure 7. (*a*) Cross-power of radial and vertical CO_2 interferometer channels showing the many RSAEs (upward-sweeping lines) and TAEs ($\sim$ horizontal lines) in the plasma. (*b*) Neutron rate and FIDA densities at $R = 180$ and 195 cm versus time. The signals are normalized by the classical TRANSP neutron and beam-ion density predictions, respectively. The absolute calibrations of the neutron and FIDA data are adjusted so that the ratio is unity in the preceding 2.3 MW discharge at 2.0 s (when the Alfvén activity is undetectable).

structures mix at frequency crossings [15] (figure 6(*c*)). For an overview of all of the Alfvén activity, the cross-power of two line-integrated interferometer signals (figure 6(*d*)) is most convenient.

Detailed comparisons of these measurements with the mode structures predicted by linear ideal MHD theory were recently reported [15, 33]. Both the electron temperature and the electron density eigenfunctions are in excellent agreement with the NOVA code [34] for the $n = 3$ TAE and the $n = 3$ RSAE. (n is the toroidal mode number.) When the frequency of a RSAE sweeps across a TAE frequency, the eigenfunctions mix [15]. The evolution of the mode structure in these frequency-crossing events is in excellent agreement with linear theory.

3. Measurements of fast-ion transport

3.1. Baseline discharge

The time evolution of the neutron and FIDA signals in the presence of strong TAE and RSAE activity is shown in figure 7. Strong reductions relative to the classical prediction are observed by both diagnostics.

The Alfvén activity flattens the fast-ion spatial profile. Both the FIDA density profile and the fast-ion pressure profile from MSE are much flatter during the strongest activity than they are later in the discharge (figure 8). Although the pressure profile peaks as the activity weakens, it is still less peaked than classically expected at 1.2 s. This is in contrast to the profiles observed in MHD-quiescent plasmas, which are in excellent agreement with the TRANSP predictions [23].

The FIDA spectrum is sensitive to the perpendicular energy distribution [23]; distorted spectra are sometimes

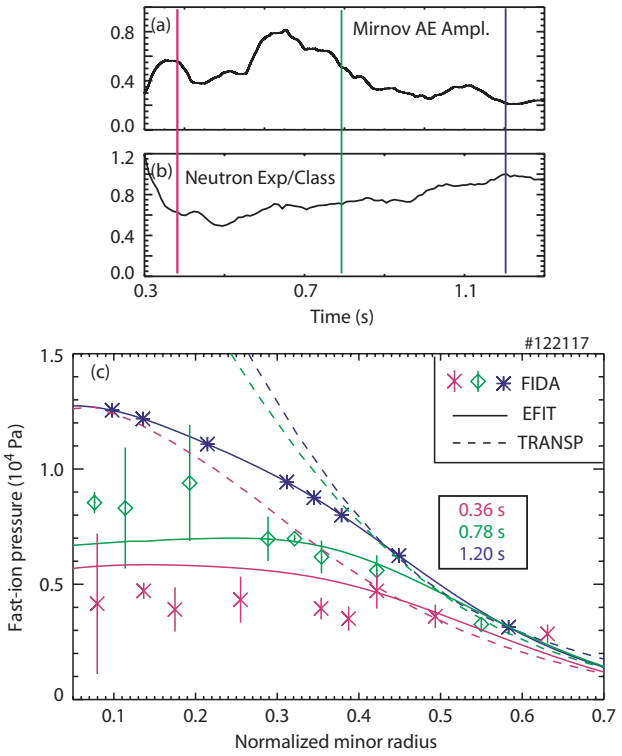

Figure 8. (*a*) Bandpass-filtered Mirnov amplitude and (*b*) neutron rate normalized to the TRANSP prediction versus time in the baseline discharge. (*c*) Fast-ion pressure profiles and FIDA density profiles versus ρ at the three indicated times. The dashed lines are the classical pressure profile predicted by TRANSP. The FIDA density profile is normalized to the MSE-EFIT p_f profile at 1.2 s.

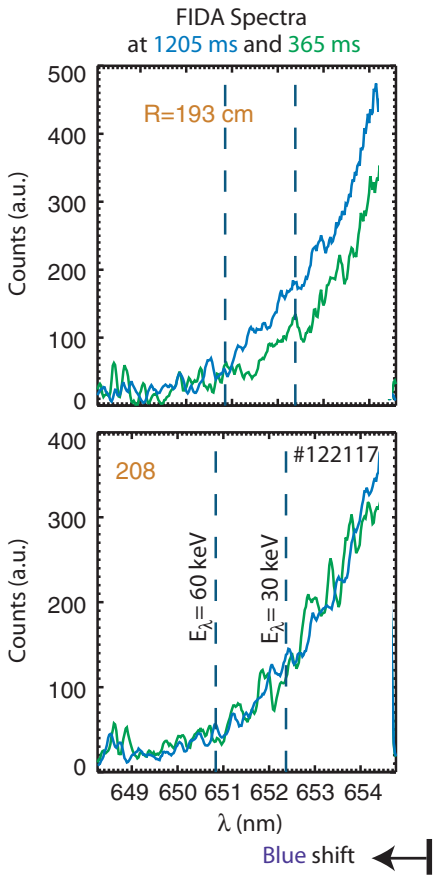

Figure 9. FIDA spectra for two channels of the Reticon diagnostic inside and outside of $\rho_{q_{min}}$. The integration windows for the FIDA density shown in the other figures are represented by dashed lines.

observed during Alfvén activity and are common during ion cyclotron heating [16]. In discharge #122117, however, the spectra agree (within the uncertainties) with the spectral shape normally observed in quiet plasmas. Figure 9 shows a few sample spectra. As this example illustrates, the steady peaking of the central fast-ion density is readily observed in the individual spectra. Since the FIDA spectra are determined by a component of the vertical motion, the approximate invariance of the spectral shape implies that the shape of the perpendicular energy distribution $\partial F/\partial E_\perp$ is not significantly altered by the Alfvén activity.

In the presence of this fast-ion transport, the plasma current diffuses more gradually than classically predicted (figure 10(*a*)). Two independent measurements of the evolution of q_{min} are in excellent agreement. They differ markedly from the classical predictions calculated by special TRANSP simulations that begin with the measured equilibrium, then evolve the current profile assuming neoclassical flux diffusion. These simulations adjust the boundary value of the parallel electric field to match the measured plasma current. For either of two extreme assumptions—either classical NBCD or no NBCD (not shown) whatsoever—the predicted diffusion is far more rapid than experimentally observed. Evidently, both the classical NBCD profile and the neoclassical conductivity profile are more peaked than the actual current profile (figure 5(*a*)). A simulation that uses the NBCD expected from a centrally flattened fast-ion density profile (figure 5(*b*)) is in better agreement with experiment (figure 10(*a*)). Apparently, the Alfvén activity redistributes circulating fast ions toward the half radius, where they contribute to a broader NBCD profile than classically expected. Gradual evolution of q_{min} was previously reported [35, 36] in more poorly diagnosed discharges. In contrast, in the preceding discharge with half the beam power and much weaker Alfvén activity (#122116), the current evolution is close to the classical expectation (figure 10(*b*)).

To estimate the experimental transport, an *ad hoc* diffusion coefficient D_B is employed in a sequence of special TRANSP runs that hold all other plasma parameters fixed. TRANSP allows the user to specify the spatial profile of D_B. Because the neutron measurement is volume-averaged, a wide variety of D_B profiles are consistent with the observed neutron rate. For example, the assumption of a spatially uniform $D_B \simeq 1.5\,m^2\,s^{-1}$ yields a predicted neutron rate that is consistent with experiment at 365 ms. On the other hand, the FIDA and p_f profile measurements provide a stronger constraint on D_B. Spatially uniform diffusion reduces the fast-ion density everywhere but results in the profile remaining peaked (figure 11). To match the flattened central profiles measured experimentally, D_B must be large in the core but become small outside $\rho \simeq 0.5$. For example, a profile that has $D_B = 5\,m^2\,s^{-1}$ in the core but falls to $D_B = 0$ near $\rho_{q_{min}}$ produces a fast-ion pressure profile that is consistent with the measured p_f profile within experimental error (figure 11). In reality, the fast-ion transport need not be diffusive nor

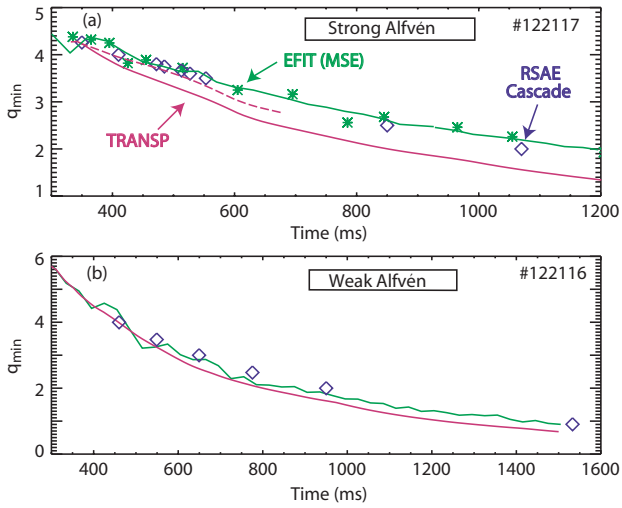

Figure 10. Measured evolution of q_{min} from MSE-based equilibrium reconstructions (line) and RSAE rational integer crossings (diamond) in discharges with (*a*) strong Alfvén activity (4.6 MW) and (*b*) weak Alfvén activity (2.3 MW). As in figure 5(*b*), the TRANSP simulations assume either classical NBCD (solid) or the NBCD from a rapidly flattened fast-ion density profile (dashed).

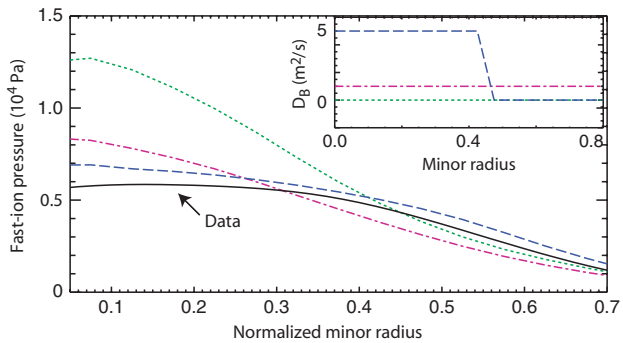

Figure 11. Measured p_f profile (solid black line) in the baseline discharge at 365 ms, together with pressure profiles computed by TRANSP assuming the three fast-ion diffusion models illustrated in the inset: no diffusion (green dotted line), spatially constant diffusion of 1 m^2 s^{-1} (red dot–dash line) and large central diffusion (blue dashed line).

apply equally to all fast ions but this empirical modelling does provide a convenient parametrization of the magnitude and spatial dependence of the actual fast-ion transport. The transport is quite large in the core and approaches classical levels outside $\rho_{q_{min}}$.

3.2. Discharges with ECH

During the 2007 campaign, an experiment was conducted to study the effect of changes in the electron temperature gradient on the RSAE activity [37]. The target discharge for this study was the baseline discharge (#122117) discussed in the previous section. Application of ECH near $\rho_{q_{min}}$ has a strong effect on the mode activity, effectively suppressing the RSAEs (figures 12(*b*) and 13(*b*)). The central FIDA signal is significantly larger when the RSAE activity is suppressed (figure 12(*c*)). Even without RSAEs, both the neutron and FIDA signals are significantly less than the classical prediction, suggesting that the TAEs also play a role in the

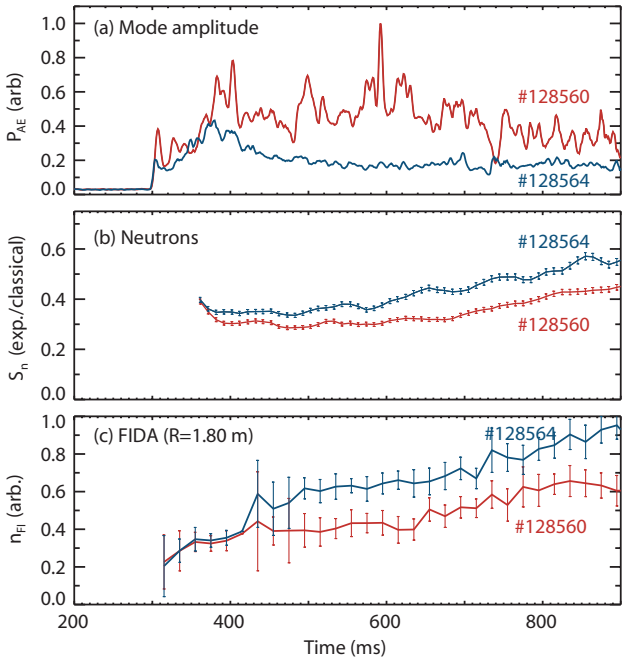

Figure 12. Time evolution of (*a*) bandpass-filtered (50–200 kHz) interferometer cross-power spectra, (*b*) neutron rate normalized to the TRANSP prediction and (*c*) central FIDA density in (red) a discharge with central ECH heating and (blue) a discharge with ECH applied near $\rho_{q_{min}}$. The error bars on the FIDA measurement are the uncertainty associated with background subtraction.

fast-ion transport. Comparison of the FIDA profiles in the discharges with and without RSAE activity confirms that the profile is flatter when both RSAEs and TAEs are present (figure 13(*c*)). This change is not an artefact of the altered electron temperature profile, as the classically predicted fast-ion profile shows the opposite trend: it is *more* peaked on the shot with RSAEs. Evidently, both RSAEs and TAEs contribute to the observed transport.

Measurements of the toroidal rotation of the plasma show additional evidence of anomalous fast-ion transport in these plasmas. The neutral beams are the dominant source of torque in these discharges. When the RSAE activity is suppressed, the central rotation is nearly twice as large as in the discharge with both TAE and RSAE activity (figure 14(*a*)). Nevertheless, if the rotation and density profiles over the entire minor radius are integrated to compute the total angular momentum, the integrated angular momentum is nearly identical in the two discharges (figure 14(*b*)). If one assumes that the thermal momentum diffusivity is not appreciably altered by the change in RSAE activity, these data suggest that, in the presence of the RSAE activity, circulating beam ions move away from the magnetic axis without being lost from the plasma. Like the FIDA and p_f profiles in the baseline discharge, the rotation data are consistent with an empirical D_B profile that is large in the core but small outside $\rho_{q_{min}}$ (figure 11). More details of this work will be reported in a forthcoming publication [38].

3.3. Correlation between fast-ion transport and Alfvén activity

Examples of the temporal correlation between reductions in fast-ion density and the strength of the Alfvén activity in

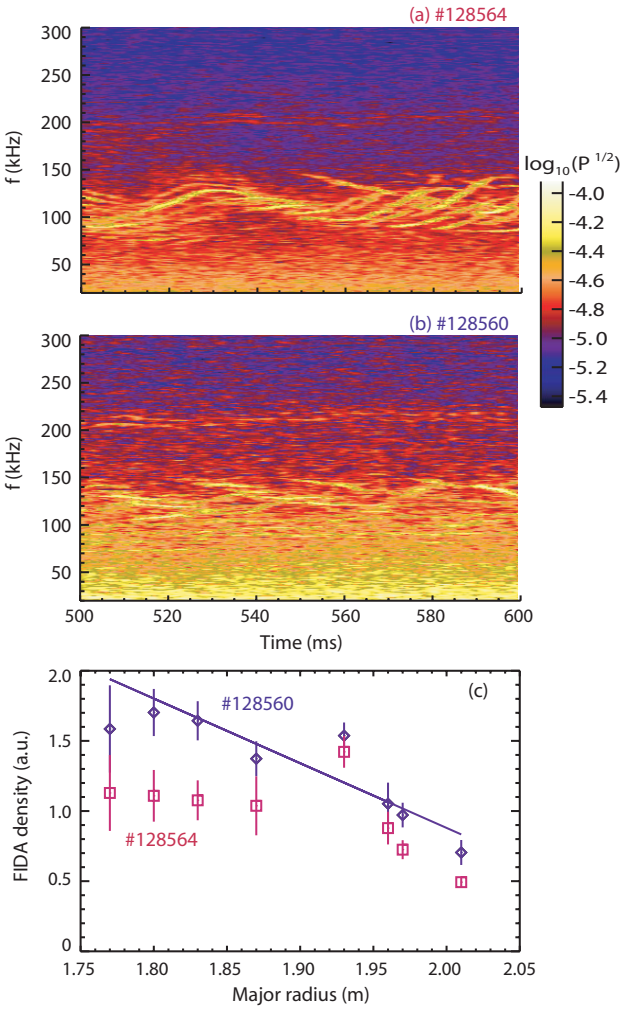

Figure 13. Interferometer cross-power spectra in (*a*) a discharge with central ECH heating and (*b*) a discharge with ECH applied near $\rho_{q_{\min}}$. The strong wavy lines in the upper spectrum are RSAEs. (*c*) FIDA density profiles averaged from 500 to 600 ms in the two discharges. The error bars represent uncertainties associated with the background subtraction; uncertainties in channel-to-channel calibration are larger but the relative change for a given position are well represented by the indicated error bars. The solid line shows the linear fit to the gradient used for the database shown in figure 17.

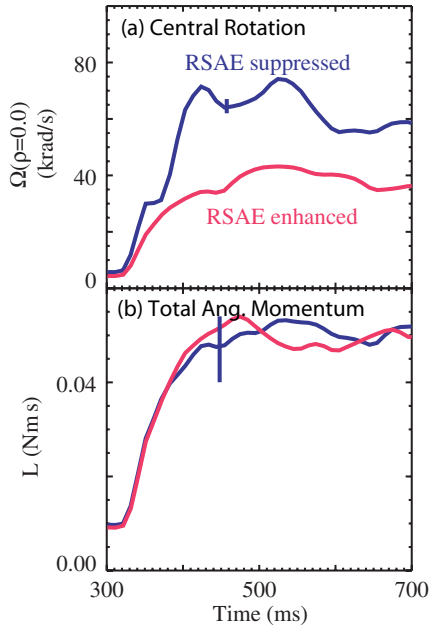

Figure 14. (*a*) Central toroidal rotation of carbon and (*b*) total toroidal angular momentum of the plasma versus time for the discharges with ECH shown in figures 12 and 13. Typical uncertainties are represented by the vertical blue lines.

individual discharges are shown in figures 7 and 12. Because of the complexity of the Alfvén activity, it is difficult to quantify the composite amplitude. The frequency band of interest spans from 0.5 to 2.0 f_{TAE}, where $f_{\mathrm{TAE}} = v_{\mathrm{A}}/4\pi q R$ is the frequency at the centre of the TAE gap. We find that three distinct measures of Alfvénic activity yield similar results. One measure of Alfvénic activity is to use the amplitude of a bandpass-filtered Mirnov signal. Another approach is to examine the entire set of 40 ECE channels, find the ten largest modes, then sum their power. A third approach is to compute the cross-power of the vertical and radial interferometer signals and record the integrated power either in the frequency band between 0.5 f_{TAE} and 2.0 f_{TAE} or between 50 and 200 kHz (similar values are obtained either way). In general, any of these approaches yields similar correlation coefficients with the measured reductions in fast-ion signal.

An example of the correlation with the bandpass-filtered magnetics signal is shown in figure 15 for a set of five sequential discharges with increasing beam power on each shot. The baseline discharge (section 3.1) is the second discharge in this sequence. As expected, the strength of Alfvén activity is smallest in the discharge with only a single beam source injecting 2.3 MW of power (figure 15(*a*)). The activity is stronger with two beam sources (the baseline discharge with 4.6 MW of power), then approximately saturates in the very strongly driven plasmas with 3, 4 and 5 sources of injected beam power. The suppression of the neutron rate and the FIDA density relative to their classical values correlates with the mode amplitudes: the suppression is smallest with one injected source, larger with two injected sources and approximately saturates at a large level for 3, 4 and 5 sources (figures 15(*b*) and (*c*)).

Data from the same five discharges are presented differently in figure 16. In this figure, the amplitude of the ten largest modes in the ECE spectra provide the measure of the strength of Alfvén activity. Rather than showing the time evolution (which is similar to the previous figure), in this figure the normalized fast-ion signals are plotted versus ECE mode amplitude. Once again, it is evident that the discrepancy between the classical prediction and the data is largest when the Alfvén modes are strong. Figure 16 also shows that the deficit in the central FIDA density is larger than the deficit in the volume-averaged neutron rate. This is consistent with the flattened spatial profiles (figure 8) and empirical D_{B} modelling (figure 11) presented earlier: flattened profiles impact the central density more than the volume-averaged neutron signal.

Figure 15(*d*) shows the signal from the loss detector that is mounted near the midplane on the vacuum vessel wall. This signal shows a dependence on beam power (especially late in the discharge) but the dependence on the amplitude of the mode

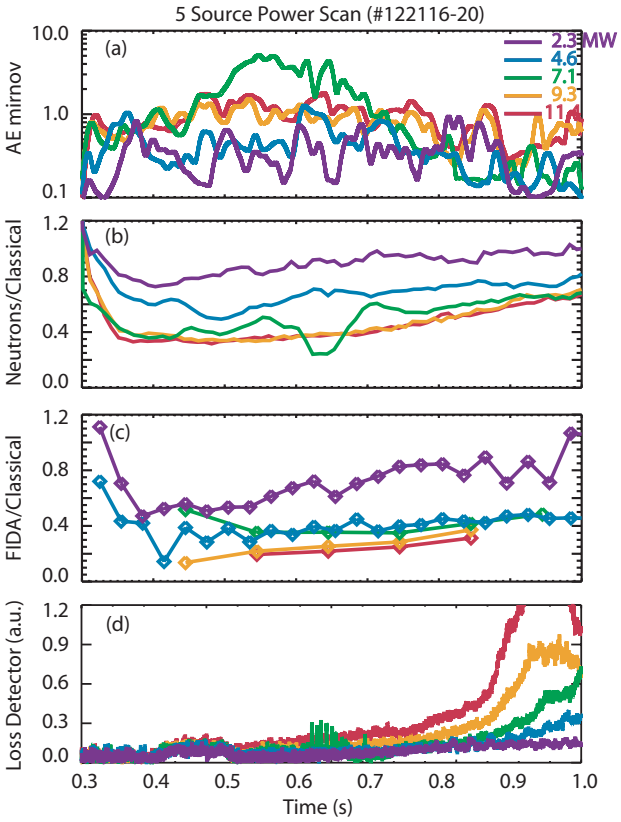

Figure 15. (*a*) Amplitude of magnetic fluctuations between 60 and 120 kHz, (*b*) ratio of the measured neutron rate to the rate predicted by TRANSP assuming neoclassical fast-ion confinement, (*c*) ratio of the FIDA signal at $R = 1.94$ m to the fast-ion density predicted by TRANSP at the same minor radius and (*d*) co-going beam-ion loss detector signal for five similar discharges with injected beam powers of 2.3, 4.6, 7.1, 9.3 and 11.4 MW, respectively.

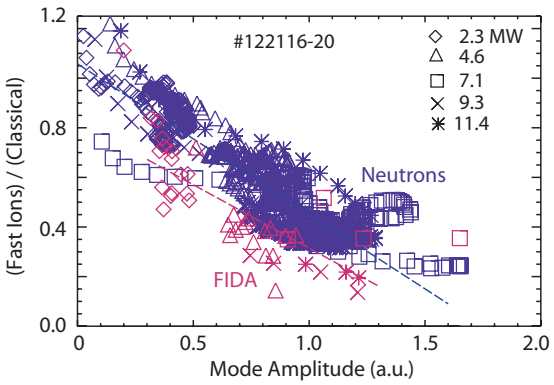

Figure 16. Normalized neutron rate and $R = 180$ cm FIDA density versus ECE mode amplitude at various times in the five successive discharges with increasing amounts of beam power shown in figure 15. The mode amplitude is obtained by summing the amplitudes of the ten largest modes measured by the ECE diagnostic in the frequency band above 50 kHz. The dashed lines are linear fits to the data.

activity is different than for the confined fast-ion diagnostics. The lack of correlation early in the discharge is consistent with the empirical D_B modelling (figure 11), which implies that most fast ions are redistributed but not lost. The rise in signal late in the discharge may reflect changes in the loss

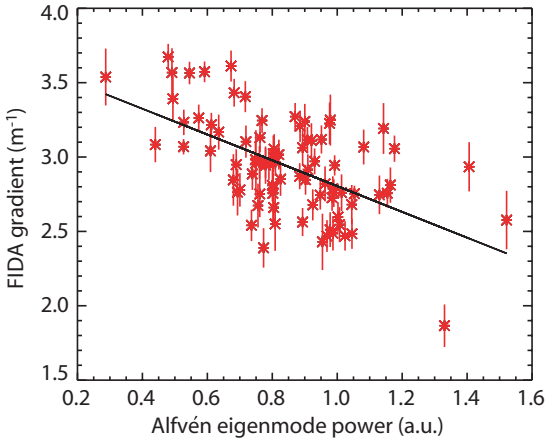

Figure 17. Gradient of the FIDA density profile (as in figure 13(*c*)) versus interferometer cross-power in the 50–200 kHz frequency band in many reversed-shear discharges from the 2006 and 2007 campaigns. The vertical error bars represent the uncertainty in slope of the linear fit to the FIDA density profile. The solid line is from a least-squares fit to the data.

orbits viewed by the detector as the plasma current evolves (figure 2(*a*)). In general, because loss detectors only measure a small portion of fast-ion phase space, definitive conclusions about fast-ion transport based on a single loss detector are problematic.

To investigate the correlation of profile flattening with Alfvén activity a database of reversed-shear discharges from the 2006 and 2007 campaigns is compiled. Time slices with fairly steady conditions are selected, with typical temporal averaging of 100 ms. The fast-ion spatial profile is measured by FIDA and a line is fit to the data as a crude measure of the slope of the profile; figure 13(*c*) shows an example. To quantify the Alfvén activity, the bandpass-filtered cross-power of the interferometers is used, as in figures 13(*a*) and (*b*). As in figures 8 and 13, the FIDA gradient is largest when the Alfvén mode power is small (figure 17), with a statistically significant correlation coefficient of $r = -0.7$. The large scatter in the fit is not unexpected, as the actual wave–particle interactions have a complex dependence on the mode eigenfunctions and frequencies whose effect cannot be adequately represented by a single mode amplitude and fast-ion gradient.

4. Simulated fast-ion transport with the ORBIT code

Fast-ion orbits in an axisymmetric tokamak are conveniently described in terms of the three constants of motion: energy E, magnetic moment μ, and toroidal canonical angular momentum $P_\zeta = mRv_\zeta - Ze\Psi$. (Here m and Ze are the ion mass and charge and Ψ is the poloidal flux.) Figure 18(*a*) shows the topological boundaries for the various types of fast-ion orbits [39] for 80 keV deuterium ions at 365 ms in the baseline discharge. Most of the fast ions are born on co-circulating orbits (figure 18(*b*)). Because of the low frequency of Alfvén modes compared with the cyclotron frequency and their relatively low amplitude, the magnetic moment μ is theoretically expected to remain conserved in the presence of the waves. The energy is expected to change but the fractional change in energy is expected to be an

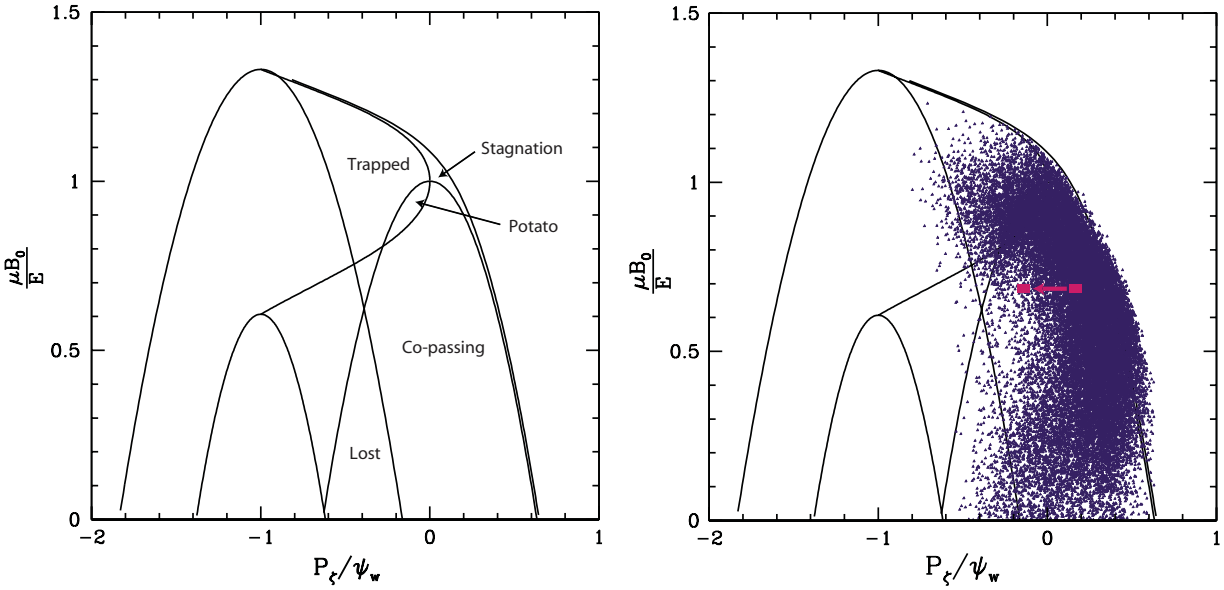

Figure 18. Orbit topology for the DIII-D baseline condition at 365 ms. The abscissa is the canonical toroidal angular momentum normalized to the poloidal flux at the last closed flux surface. The ordinate is the magnetic moment normalized by the field at the magnetic axis B_0 and the energy E. The different types of orbits in various regions are indicated in the left graph, while the location of the birth distribution of orbits computed by TRANSP is shown in the right graph. The red arrow indicates a typical trajectory for a circulating beam ion that ionizes near the magnetic axis and is transported to the half radius by Alfvén activity.

order of magnitude smaller than the fractional change in P_ζ. Because P_ζ decreases with increasing poloidal flux Ψ, movement outward from the magnetic axis corresponds to a reduction in P_ζ. Thus, a typical particle that is redistributed from the magnetic axis out to the half radius is expected to execute leftward motion similar to the trajectory illustrated in figure 18(*b*).

To compute the expected transport by the Alfvén modes, the initial fast-ion birth distribution function F_0 is obtained from a short (1 ms) TRANSP run that models the beam deposition and initial orbits but is too short for Coulomb collisions to appreciably alter the distribution. The initial distribution function obtained from this TRANSP run is shown in figure 18(*b*). The expected effect of the modes on these particles is calculated by the Hamiltonian guiding centre code ORBIT [40]. Transverse shear Alfvén waves with negligible parallel electric and magnetic fields $E_\parallel$ and $B_\parallel$ are assumed, so a single scalar field α describes the perturbed fields, $\delta \boldsymbol{B} = \nabla \times \alpha \boldsymbol{B}_0$ [39]. The eleven strongest toroidal modes in the TAE/RSAE range of frequencies are matched to NOVA linear eigenfunctions and the amplitudes are scaled to agree with the ECE measurements. The selected modes are shown in figure 19(*a*). Reliable mode identification is possible for the largest 7–8 modes but is problematic for the weakest ones or for modes with similar frequencies. For each toroidal mode, the strongest poloidal harmonics m are selected and a total of 151 $\alpha_{m,n}$ helical perturbations with their experimental amplitudes and frequencies are entered into ORBIT. The α representation of one of the eleven modes is shown in figure 19(*b*). (This particular mode is a RSAE whose frequency has risen sufficiently that it has converted into a TAE with odd parity in the high frequency side of the TAE gap.) The peak amplitude of this ∼101 kHz mode is $\Delta T_e = 3\,\mathrm{eV}$, $B_r/B_0 \sim 1 \times 10^{-3}$ and $\alpha_{26,7} = 2 \times 10^{-6}$. Evolution of the frequency and mode structure is ignored since these barely change on orbital timescales. The particle orbits are computed in the presence of pitch-angle scattering and the perturbed fields, then the distribution function F is sampled for comparison with F_0.

This procedure cannot account for the observed fast-ion transport. Figure 20 shows the change in the distribution function in the region of velocity space that makes the dominant contribution to the measured fast-ion signals for ORBIT runs where the mode amplitudes are artificially enhanced by a factor of five. Even with this enormous enhancement, which is much larger than the experimental uncertainty of $\lesssim$10%, the transport is smaller than observed. The ORBIT simulations predict transport in the correct locations but, even with five times the measured amplitude, the change in the distribution function is far smaller than the empirically observed level derived from TRANSP simulations with *ad hoc* diffusion. The predicted transport is comparable to neoclassical diffusion.

5. Discussion

The discrepancy between ORBIT simulations and the observed transport indicate that something is missing in the simulations. In this section, we list and evaluate several possibilities.

- *The measured mode amplitude is too small.* This explanation is very unlikely. As shown in [33], the mode amplitude derived from the ECE measurements of T_e are consistent with independent measurements of n_e by the BES and reflectometer diagnostics. The RSAE and TAE mode amplitudes are not ten times larger than measured.
- *The measured fast-ion transport is too large.* This explanation is also very unlikely. As shown in section 3, five independent fast ion diagnostics (neutrons, FIDA, p_f, current profile, toroidal rotation) all indicate strong transport under these conditions. All five measurements

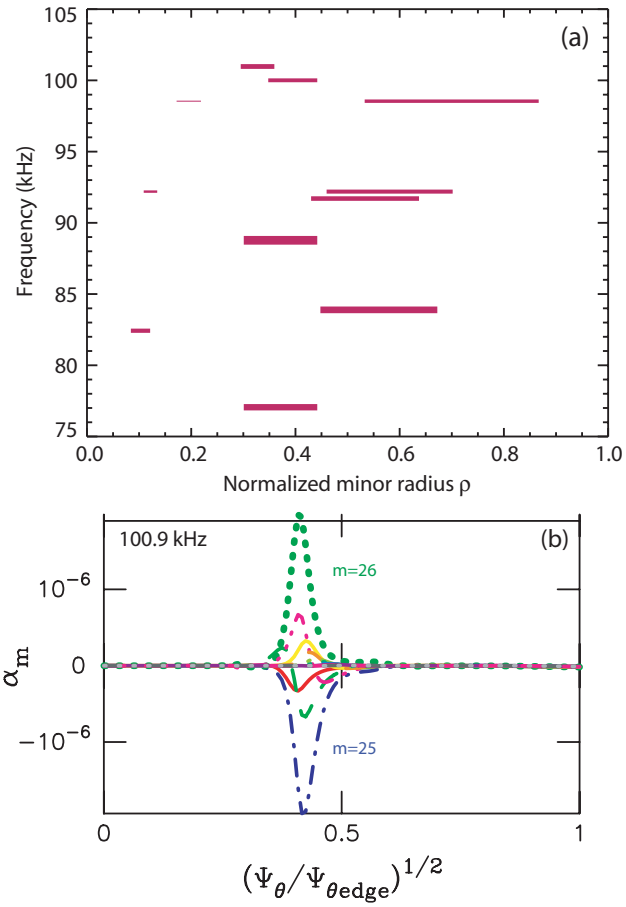

Figure 19. (*a*) The eleven toroidal modes used in the ORBIT calculations. The frequency of the mode is represented by its vertical position, the peak amplitude of the mode by the width of the line, and the radial extent ($1/e$ locations) by the horizontal length of the line. (*b*) Poloidal α harmonics of the $n = 7$, 101 kHz mode.

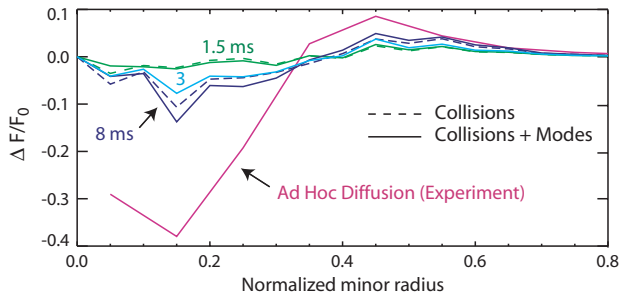

Figure 20. Change in the distribution function of fast ions with $E \geqslant 60$ keV and $v_\parallel/v = 0.4$–0.7 versus ρ; ΔF is normalized to the maximum value of the intial distribution function, which occurs at $\rho = 0.15$. The dashed lines are with collisions alone; the solid lines include collisions and 151 helical modes at five times the experimental amplitudes for the TAEs and RSAEs that are observed at 356 ms. The distribution function is sampled after 0.95–1.9 ms (green), 1.9–3.8 ms (turquoise) and 5.5–11 ms (purple). The red curve compares a TRANSP simulation with $D_B = 5\ m^2\ s^{-1}$ inside $\rho = 0.55$ and zero outside with a standard ($D_B = 0$) simulation. To approximate the conditions of the 8 ms ORBIT simulation, F is evaluated for $E > 66$ keV, since an 80 keV deuteron slows down to 66 keV in 8 ms under these conditions.

require similar levels of *ad hoc* beam-ion diffusion to explain the observations.

- *ORBIT only follows drift orbits, not the full gyro-orbit.* The fast-ion gyroradius is only $\rho_f = 2$ cm and the conditions for gyro-averaging seem well satisfied, so this explanation is also very unlikely. The equations employed for the drift orbits in ORBIT are not exact [41] but estimates indicate that the incurred error is very small for these conditions.
- *Toroidal field ripple is neglected.* Modelling indicates that ripple transport in conjunction with TAEs [42] was responsible for damage to the TFTR vessel but the DIII-D tokamak has 24 relatively distant toroidal field coils, so the central ripple is only $\sim 2 \times 10^{-6}$ and is unlikely to cause appreciable transport.
- *ORBIT assumes* $\delta B_\parallel = 0$. No measurements of the polarization of the modes are available but β is modest; estimates based on parallel pressure balance [43] suggest that the energy exchange associated with magnetic mirroring effects is on the order of 1% of the energy exchange associated with the $\boldsymbol{v}_d \cdot \boldsymbol{E}_\perp$ term that is included in the ORBIT simulations. (Here, $\boldsymbol{v}_d$ is the drift velocity away from the flux surface and $\boldsymbol{E}_\perp$ is the transverse electric field of a shear Alfvén wave.)
- *ORBIT assumes* $\delta E_\parallel = 0$. This is an excellent assumption for shear Alfvén waves with $\omega \ll \Omega_{ci}$ as long as the waves do not interact with the Alfvén continuum. As shown in [15], the continuum gap structure is quite open early in the beam injection, so this assumption seems reasonable.
- *The modelling neglects mixing of the RSAE and TAE eigenfunctions.* In reality, when the frequency of a RSAE sweeps through the frequency of a TAE, the eigenfunctions mix [15]. For simplicity, we selected a time where the eigenfunctions are not mixed for the ORBIT modelling. Evidence of frequency crossings are clearly evident in the Mirnov coil data, confirming that the global extent of some modes increases at these times. The effect of occasional mixing of the eigenfunctions on fast-ion transport has not been computed yet.
- *The modelling used fixed frequency modes.* Resonant particles that are trapped in a finite amplitude wave can experience convective transport when the wave chirps in frequency [44]. Estimates based on equation (5*a*) of [44] suggest that frequency chirping of the RSAEs could cause appreciable transport. Numerical calculations of this effect are planned.
- *EPMs contribute significantly to the transport.* Although there is a clear correlation of fast-ion transport with RSAE and TAE amplitude (section 3.3), it is possible and perhaps even likely that the amplitude of other modes are also correlated with the RSAE and TAE amplitudes. Modelling of JT-60U discharges with intense beam injection finds energetic particle modes (EPMs) with frequencies that sweep rapidly in time and space in addition to TAEs [45]. In both simulation and experiment, these EPMs produce an order of magnitude more fast-ion transport than the TAEs. Similar simulations of our baseline discharge find EPMs, RSAEs and TAEs but the EPMs cause appreciably more transport than the RSAEs and TAEs [46]. Using wavelet analysis of the

interferometer signals, we have searched for evidence of transient EPMs in the baseline discharge but have not found any evidence for intense EPM activity.

- *Coherent low frequency modes cause appreciable transport.* There are no neoclassical tearing modes or fishbones in these discharges but many unidentified modes with frequencies $\lesssim 0.5 f_{\mathrm{TAE}}$ do appear in the spectra. Figure 21 shows some typical examples. Some of these modes are probably beta-induced Alfvén eigenmodes (BAEs) [47] or beta-induced Alfvén-acoustic eigenmodes (BAAEs) [48]. In general, the amplitude of these modes is comparable to the modelled RSAEs and TAEs.
- *Incoherent (turbulent) modes cause appreciable transport.* Generally, the signal level on all of the fluctuation diagnostics increases in a band that extends up to the frequency of geodesic acoustic modes (GAMs),

$$f_{\mathrm{GAM}} = \frac{\sqrt{2(T_{\mathrm{e}} + 7T_{\mathrm{i}}/4)/m_{\mathrm{i}}}}{R}. \qquad (1)$$

Figure 21(*b*) shows a typical example. Comparison of the auto-power from one coil with the cross-power from a pair of probes that are separated by 45° toroidally shows that the power in this low-frequency band contains roughly equal contributions of coherent peaks and incoherent noise.

It is instructive to compare our calculations of fast-ion transport with earlier studies. Sigmar *et al* [49] found substantial losses of super-Alfvénic alphas in a slowing-down time for a global, low-n TAE when the mode amplitude B_r/B_0 exceeded 10^{-3}, i.e. a level comparable to our experimentally observed amplitude. Appel *et al* [50] found appreciable diffusion of super-Alfvénic alphas when the TAE or kinetic TAE amplitude was $\gtrsim 4\times10^{-3}$. In simulations of a global TAE, Todo and Sato [51] found appreciable alpha particle transport for mode amplitudes similar to Sigmar *et al*. In the simulations of Candy *et al* [52], a single dominant TAE grew to a very large amplitude of $B_r/B_0 > 10^{-2}$. In simulations of beam-ion transport, Carolipio *et al* computed losses of a few percent for global TAEs at an amplitude of $B_r/B_0 = 4 \times 10^{-3}$. In their simulations of the first beam-driven TFTR experiments, Todo *et al* [6] calculated saturated mode amplitudes in excess of 10^{-2}. All of these simulations made assumptions about the mode polarization similar to ours. In summary, based on previous work, with the mode amplitude enhanced five times over the experimental level, one expects appreciable fast-ion transport. Consistent with that expectation, some transport is observed in our simulations but the magnitude of the transport is still below the experimental level.

Since the Lorentz force law surely holds, the modelled electric and magnetic fields must not match the fields that cause fast-ion transport in the experiment. Even though the TAE and RSAE measurements agree well with the eigenfunction computed by ideal MHD, one possibility is that the RSAEs and TAEs actually have appreciable values of $E_{\parallel}$. Another possibility is that the waves that dominant the transport are strongest when the RSAE and TAE activity is strong, resulting in a misleading correlation between flattening of the fast-ion profile and the mode amplitude in the TAE band. In particular, the many modes with frequencies below the GAM frequency may dominate the fast-ion transport.

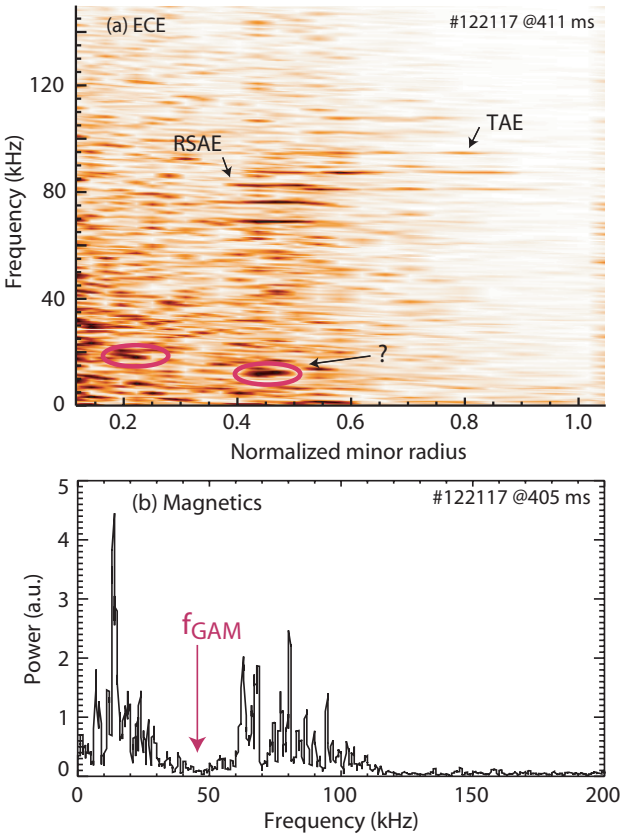

Figure 21. (*a*) Radial profile of T_{e} fluctuations constructed from the ECE spectra at 411 ms in the baseline discharge. Two unidentified low frequency modes are indicated. (*b*) Auto-power spectrum of the magnetics signal at 405 ms. The GAM frequency near $\rho_{q_{\mathrm{min}}}$ is also indicated.

6. Conclusions

In conclusion, five independent diagnostics all indicate strong transport of fast ions in reversed-shear discharges with multiple TAE and RSAE modes. In quiet plasmas, these same diagnostics agree with classical [23] and ion cyclotron [16] theory. Moreover, similar profiles are measured with different techniques during Alfvén activity in reversed shear plasmas on JT-60U [53]. The mode amplitudes are also measured by four independent diagnostics [33]. The hypothesis that diagnostic inadequacies account for the discrepancy between theory and experiment is therefore excluded. Fast-ion transport is remarkably effective in plasmas with Alfvén activity.

Calculations of the expected fast-ion transport based on MHD modelling of the RSAEs and TAEs do not account for the strong transport. Identification of the mechanism responsible for this transport is an urgent task in burning plasma physics. Planned experiments on DIII-D will focus on simplifying the experimental conditions by reducing the number of unstable modes.

Acknowledgments

The assistance of the DIII-D team and helpful discussions with Liu Chen, J. Ferron, C. Petty, and G. Vlad are

gratefully acknowledged. Wavelet software was provided by C. Torrence and G. Compo, and is available at URL: http://paos.colorado.edu/research/wavelets/.

This work was funded by US DOE subcontract SC-G903402 to US DOE contract DE-FC02-04ER54698 and DE-AC02-76CHO3073, DE-FG03-97ER54415, W-7405-ENG-48 and DE-FG02-89ER53296.

References

[1] Gorelenkov N.N. *et al* 2003 *Nucl. Fusion* **43** 594
[2] Cheng C.Z., Chen L. and Chance M. 1985 *Ann. Phys.* **161** 21
[3] Duong H.H. *et al* 1993 *Nucl. Fusion* **33** 749
[4] White R.B. *et al* 1995 *Phys. Plasmas* **2** 2871
[5] Carolipio E.M. *et al* 2001 *Phys. Plasmas* **8** 3391
[6] Todo Y. *et al* 2003 *Phys. Plasmas* **10** 2888
[7] Heidbrink W.W. *et al* 2007 *Phys. Rev. Lett.* **99** 245002
[8] Sharapov S.E. *et al* 2002 *Phys. Plasmas* **9** 2027
[9] Betti R. and Freidberg J.P. 1992 *Phys. Fluids* B **4** 1465
[10] Biglari H., Zonca F. and Chen L. 1992 *Phys. Fluids* B **4** 2385
[11] Carlstrom T.N. *et al* 1992 *Rev. Sci. Instrum.* **63** 4901
[12] Austin M.E. and Lohr J. 2003 *Rev. Sci. Instrum.* **74** 1457
[13] Carlstrom T.N., Ahlgren D.R. and Crosbie J. 1998 *Rev. Sci. Instrum.* **59** 1063
[14] Gohil P., Burrell K.H., Groebner R.J. and Seraydarian R.P. 1990 *Rev. Sci. Instrum.* **61** 2949
[15] Van Zeeland M.A. *et al* 2007 *Phys. Plasmas* **14** 056102
[16] Heidbrink W.W. *et al* 2007 *Plasma Phys. Control. Fusion* **47** 1457
[17] Heidbrink W.W., Taylor P.L. and Phillips J.A. 1997 *Rev. Sci. Instrum.* **68** 536
[18] Budny R.V. 1994 *Nucl. Fusion* **34** 1247
[19] Luo Y., Heidbrink W.W., Burrell K.H., Kaplan D.H. and Gohil P. 2007 *Rev. Sci. Instrum.* **78** 033505
[20] Egedal J. and Bindslev H. 2004 *Phys. Plasmas* **11** 2191
[21] Whyte D.G. *et al* 1998 *Nucl. Fusion* **38** 387
[22] Luo Y., Heidbrink W.W. and Burrell K.H. 2004 *Rev. Sci. Instrum.* **75** 3468
[23] Luo Y., Heidbrink W.W., Ruskov E., Burrell K.H. and Solomon W.M. 2007 *Phys. Plasmas* **14** 112503
[24] Rice B.W., Nilson D.G., Burrell K.H. and Lao L.L. 1999 *Rev. Sci. Instrum.* **70** 815
[25] Lao L.L., St John H., Stambaugh R.D., Kellman A.G. and Pfeiffer W. 1985 *Nucl. Fusion* **25** 1611
[26] Petty C.C. *et al* 1997 Fast wave current drive in neutral beam heated plasmas on DIII-D *Proc. 12th Int. Conf. on Radio Frequency Power in Plasmas (Savannah, GA, 1997)* (New York: AIP) p 225
[27] Heidbrink W.W. *et al* 1999 *Nucl. Fusion* **39** 1369
[28] Cecil F.E. *et al* 2003 *Rev. Sci. Instrum.* **74** 1743
[29] Wang G. *et al* 2006 *Nucl. Fusion* **46** S708
[30] Gupta D.K., Fonck R.J., Mckee G.R., Schlossberg D.J. and Shafer M.W. 2004 *Rev. Sci. Instrum.* **75** 3493
[31] Van Zeeland M.A. *et al* 2005 *Plasma Phys. Control. Fusion* **47** L31
[32] Strait E.J. 1996 *Rev. Sci. Instrum.* **67** 2538
[33] Van Zeeland M.A. *et al* 2006 *Phys. Rev. Lett.* **97** 135001
[34] Cheng C.Z. 1992 *Phys. Rep.* **1** 211
[35] Wong K.L. *et al* 2004 *Phys. Rev. Lett.* **93** 085002
[36] Wong K.L. *et al* 2005 Nucl. Fusion **45** 30
[37] Van Zeeland M.A. *et al* 2008 *Plasma Phys. Control. Fusion* **50** 035009
[38] Solomon W. *et al* 2008 *Plasma Phys. Control. Fusion* **49** to be submitted
[39] White R.B. 2001 *The Theory of Toroidally Confined Plasmas* 2nd edn (London: Imperial College Press)
[40] White R.B. and Chance M.S. 1984 *Phys. Fluids* **27** 2455
[41] Cooper G.A., Jucker M., Cooper W.A., Graves J.P. and Isaev M.Y. 2007 *Phys. Plasmas* **14** 102506
[42] White R.B. *et al* 1995 *Nucl. Fusion* **35** 1707
[43] Chen L. and Zonca F. 2007 *Nucl. Fusion* **47** S727
[44] Hsu C.T., Cheng C.Z., Helander P., Sigmar D.J. and White R. 1994 *Phys. Rev. Lett.* **72** 2503
[45] Briguglio S., Fogaccia G., Vlad G. and Zonca F. 2007 *Phys. Plasmas* **14** 055904
[46] Vlad G. 2007 *10th IAEA Technical Meeting on Energetic Particles in Magnetic Confinement Systems (Kloster Seeon, 8–10 October 2007)* (Paper OT 7)
[47] Turnbull A.D. *et al* 1993 *Phys. Fluids* B **5** 2546
[48] Gorelenkov N. 2007 *Phys. Lett.* A **370–371** 70
[49] Sigmar D.J., Hsu C.T., White R. and Cheng C.Z. 1992 *Phys. Fluids* B **4** 1506
[50] Appel L.C. *et al* 1995 *Nucl. Fusion* **35** 1697
[51] Todo Y. and Sato T. 1998 *Phys. Plasmas* **5** 1321
[52] Candy J., Berk H.L., Breizman B.N. and Porcelli F. 1999 *Phys. Plasmas* **6** 1822
[53] Ishikawa M. *et al* 2007 *Nucl. Fusion* **47** 849